



A scanning reflection X-ray microscope for magnetic imaging in the EUV range

Andreas Schümmmer,^{a*} H.-Ch. Mertins,^a Claus Michael Schneider,^b Roman Adam,^b Stefan Trellenkamp,^b Rene Borowski,^b Daniel Emil Bürgler,^b Larissa Juschkina^b and Ulf Berges^c

Received 12 April 2019

Accepted 3 September 2019

^aFH-Münster, Stegerwaldstraße 39, 48565 Steinfurt, Germany, ^bForschungszentrum Jülich, Wilhelm-Johnen-Straße, 52428 Jülich, Germany, and ^cZentrum für Synchrotronstrahlung DELTA, Maria-Goeppert-Mayer-Straße, 44227 Dortmund, Germany. *Correspondence e-mail: a.schuemmer@fh-muenster.de

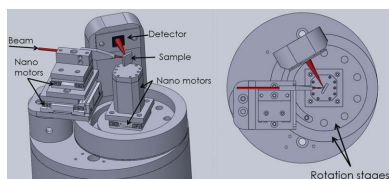
Edited by S. Svensson, Uppsala University, Sweden

Keywords: magnetism; microscopy; X-ray; synchrotron; zone plates.

The mechanical setup of a novel scanning reflection X-ray microscope is presented. It is based on zone plate optics optimized for reflection mode in the EUV spectral range. The microscope can operate at synchrotron radiation beamlines as well as at laboratory-based plasma light sources. In contrast to established X-ray transmission microscopes that use thin foil samples, the new microscope design presented here allows the investigation of any type of bulk materials. Importantly, this permits the investigation of magnetic materials by employing experimental techniques based on X-ray magnetic circular dichroism, X-ray linear magnetic dichroism or the transversal magneto-optical Kerr effect (T-MOKE). The reliable functionality of the new microscope design has been demonstrated by T-MOKE microscopy spectra of Fe/Cr-wedge/Fe trilayer samples. The spectra were recorded at various photon energies across the Fe 3*p* edge revealing the orientation of magnetic domains in the sample.

1. Introduction

X-ray microscopy is an important experimental technique in many scientific fields including physics, material science, chemistry and biology (Bracco & Holst, 2013; Adam *et al.*, 2005; Andrews *et al.*, 2010). The great advantages of microscopy in the X-ray spectral region are high spatial resolution down to 15 nm (Mobilio *et al.*, 2015), tunable penetration depth to investigate buried layers and the availability of element- and magnetic-contrast techniques. Element selectivity is achieved by selecting an energy range for the radiation that spans a resonance energy of the element, *i.e.* by measuring at absorption edges, where resonantly enhanced signals are obtained (Späth *et al.*, 2015; Attwood & Sakdinawat, 2017; Stöhr & Siegmann, 2006). Magnetic selectivity results from the interaction of polarized light with magnetic matter. This can be exploited in measurements of the transversal magneto-optical Kerr effect (T-MOKE) or X-ray magnetic circular dichroism (XMCD), performed at relevant absorption edges (Stöhr & Siegmann, 2006; Mertins *et al.*, 2005; Kuch *et al.*, 2015; Hubert & Schäfer, 1998). Due to the resonant enhancement occurring at these absorption edges the magneto-optical effects are much larger in the soft X-ray and extreme ultraviolet (EUV) region than they are in the visible range (Stöhr & Siegmann, 2006; Tesch *et al.*, 2013). Furthermore, magneto-optical effects that are quadratic in the magnetization, like X-ray magnetic linear dichroism (XMLD) (Stöhr & Siegmann, 2006; Mertins *et al.*, 2005; Kuneš *et al.*, 2004; Tesch *et al.*, 2014), allow the investigation of anti-



© 2019 International Union of Crystallography

ferromagnetic layers which are technologically important. An important example is their use in reading heads for magnetic data storage (Oppeneer *et al.*, 2003).

Historically the well established zone-plate-based X-ray microscopy in transmission mode is applied in the soft X-ray photon range within the so-called water window (282–533 eV) (Kirz *et al.*, 1995) and in the soft X-ray range near the $2p$ edges of transition metals (approximately 0.7–1.5 keV) (Kirz *et al.*, 1995). State-of-the-art X-ray transmission microscopes in transmission mode allow for enhanced time-resolved imaging with high spatial resolution (Johnson *et al.*, 2019; Berges *et al.*, 2007; Ruoss *et al.*, 2016). These transmission microscopes work in full-field imaging mode (TXM) or scanning mode (STXM). Importantly, the transmission mode requires thin specimens. This is a considerable disadvantage of the technique. X-ray microscopy of thick bulk samples, as they are common in industry, is not possible. Therefore, for these bulk samples only investigations in reflection mode are possible. Furthermore, buried layers are typically so deep inside the sample that microscopy in transmission mode is impossible. These limitations of the established X-ray microscopy using transmission mode may, however, be overcome by adapting a zone-plate X-ray microscope, so that it permits microscopy in reflection mode.

One particular technological challenge of X-ray microscopy in reflection mode is the development of a zone plate design that provides for a relatively long focal length. This is necessary to allow reflected light to follow a direct optical path to the detector that is not obscured by any technical elements of the setup of the microscope.

In a first proof of this concept a TXM microscope was modified to permit measurements in reflection mode by Denbeaux *et al.* (2005). This modified TXM was used to image a lines-and-spaces structure in reflection mode. In order to permit comparisons, the work presented here, which was performed in reflection mode using a novel device design, includes data for a similar test structure. These data demonstrate the spatial resolution of the novel device. The efficacy of this device is then further demonstrated by presenting data from applying the device in element-selective and magnetic imaging.

A particular challenge of magneto-optical reflection microscopy is related to the photon energy range. Typically, magneto-optical spectroscopy is applied in the soft X-ray region of the $2p$ absorption edges of transition metals with strong magneto-optical effects (Aken *et al.*, 1999) but with very low reflectance (Mertins *et al.*, 2002, 2005) limiting the application to transmission geometry. This can be solved by using photons from the lower-energy EUV range. In particular, the $3p$ absorption edges of transition metals in the EUV energy range are suitable. At these relatively low photon energies of about 50–70 eV the reflectance is two to three orders of magnitude larger than it is in the soft X-ray range at the relevant $2p$ edges. This can provide much stronger magnetic signals. Importantly, this enables X-ray microscopy at much larger angles of incidence of up to 45° where strong T-MOKE signals can be obtained (Mertins *et al.*, 2005; Hecker

et al., 2005). Furthermore, the common distortion of images at small grazing incidence angles due to the tilted sample can be reduced for such larger angles close to normal incidence.

In this paper we discuss the design, setup and mechanics of a novel device that has been developed for scanning reflection X-ray zone-plate microscopy (SRXM) and works in reflection mode rather than in transmission mode. The device is designed to operate in the EUV regime of about 30–90 eV allowing magneto-optical microscopy near the $3p$ absorption edges of magnetic $3d$ transition metals like Fe, Co and Ni. First experimental results on thin Fe films and on Fe/Cr-wedge/Fe trilayer samples are shown to demonstrate reliable and effective operation of the novel design.

2. Experimental setup

The experimental station for SRXM developed in this work is compact, easily transportable and can be operated with plasma light sources or higher harmonics sources (Mann *et al.*, 2019; Johnson *et al.*, 2019) at small research laboratories as well as with intense radiation at large-scale synchrotron facilities. Results presented in this paper have been obtained at the synchrotron facility DELTA in Dortmund at beamline 12 (Berges *et al.*, 2007). The SRXM instrument, shown in Figs. 1, 2 and 3, comprises the zone plate assembly with holder and positioning system, the aperture, the rotatable sample holder including the magnetization device, the intensity detectors and beam diagnostics. The various elements of the design are described in detail in the following sections.

2.1. SRXM chamber and optical geometry

The device is located in an ultra-high-vacuum chamber of diameter 300 mm. The optical axis is defined by the position of two apertures positioned at the front and at the end of the chamber. Using these two pinholes the chamber can be aligned manually to the light beam with a lateral accuracy of $\pm 100 \mu\text{m}$ and an angular accuracy of $\pm 1 \text{ mrad}$. The microscopy unit is placed in the centre of the chamber (Fig. 1), pre-aligned with respect to the optical axis of the chamber. The microscopy unit is compact and can be installed in any vacuum chamber with ports of 150 mm diameter. It consists of the zone plate holder mechanics in front of the sample holder (Figs. 1 and 2) which carries a magnetic coil providing a vertical magnetic field (Fig. 3). Optics and sample are adjustable by nano-motors (details see below). The sample holder is mounted on a non-commercial two-circle goniometer which allows for rotation about a vertical axis. This permits the setting of the angle of light incidence θ (Fig. 2). The angular range is from $\theta = 30^\circ$ to 60° measured with respect to the sample surface. In this paper all experiments were performed at $\theta = 30^\circ$.

The detector is mounted on the second goniometer stage with identical rotation axis. It is rotated on the horizontally reflected beam by varying the angle 2θ between 60° and 120° . For beam optimization the sample can be moved out of the beam, and the detector can be set to any angle between 0°

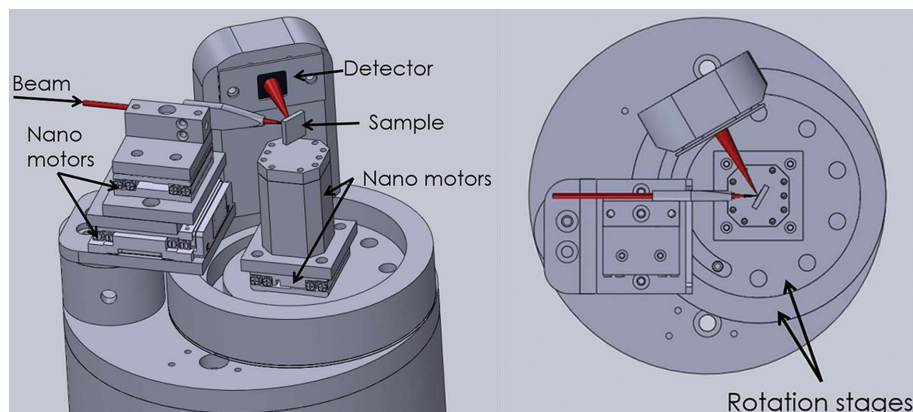


Figure 1
Principle setup of the novel SRXM instrument with optical path and components shown. For clarity the sample holder is not shown in detail. The largest possible sample diameter is 140 mm.

and 180° . The 2θ -circle allows for implementation of several detectors. Typically, a conventional channel plate detector is used. It has a dark current of 1 pA and a dynamic range up to 10 nA – this suits our signal range from 50 pA to 5 nA. The micro-channel plate provides two important advantages. Firstly, a high amplification and good signal to noise ratio

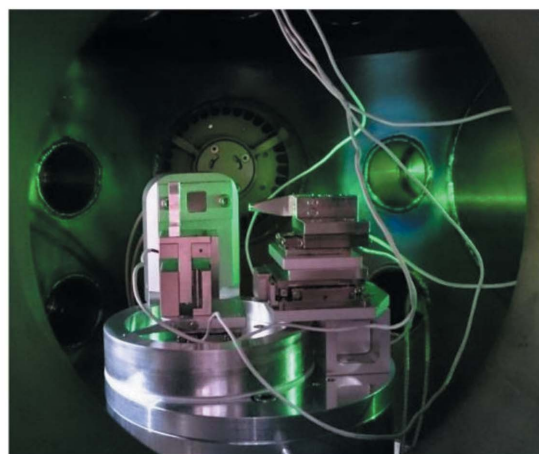
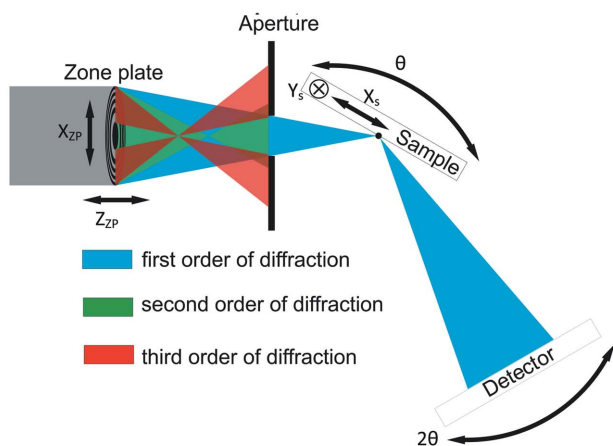


Figure 2
Top: principle setup of the novel SRXM device. The working principle of the central beam stop is only illustrated for third-order diffraction. Bottom: photograph of the microscope unit of the instrument.

is obtained compared with regular photodiodes. Secondly, this type of detector is insensitive to infrared radiation produced by the nano-motor control system (see below).

2.2. Microscope adjustment and stepper motors

The microscope operates in scanning mode where the zone plate creates a focal point of the radiation on the sample while the reflected radiation is monitored by the channel plate detector. Therefore, the zone plate has to be adjusted to both the incident light beam and the sample position. This is performed by two nano-motor stages,

one moving perpendicularly (indicated in Fig. 2 as X_{ZP}) to the beam and the other moving parallel to the beam in order to adjust the focal point at the sample surface (indicated in Fig. 2 as Z_{ZP}). The vertical (Y) alignment of the zone plate with respect to the beam is performed by manually moving the complete chamber including the microscopy unit by inching it via fine screw-actuators with an accuracy of at least $\pm 10 \mu\text{m}$.

Some zone plates have been designed to work with a central beam stop (CBS). This beam stop is shown in Fig. 2 and the resulting path is indicated for third-order diffraction. Additionally, to suppress higher-order diffraction, an aperture is used (Fig. 2). The aperture shows a diameter of $50 \mu\text{m}$ which is adopted to the diameter of the central beam stop.

The sample is scanned in an x - y direction through the light spot by two different piezo-driven nano-motors from Attocube (<https://www.attocube.com/en>). One nano-motor shows a possible minimum horizontal step size $\Delta x = 100 \text{ nm}$ and a total scanning range of 20 mm. The second nano-motor shows a minimum vertical step size $\Delta y = 50 \text{ nm}$ over a total range of 12 mm. During a scan identical step sizes are applied for vertical and horizontal directions. The accuracy and reproducibility of the nano-motor positioning system has been checked by means of interferometry using green laser light. The results confirm the manufacturer's specification of an accuracy of 5%.

2.3. Magnetization

For in-plane magnetization of the sample a coil system consisting of PTFE isolated Cu wires and an iron yoke has been developed (Fig. 3). The system creates tunable vertical magnetic fields of up to $\pm 16 \text{ mT}$. By using linearly p -polarized synchrotron radiation, T-MOKE microscopy can be performed (Fig. 3).

2.4. Zone plates

Various zone plates have been developed for the EUV range as described in a previous paper by us (Schümmer *et al.*, 2018). These were optimized for use at a wavelength of 20.6 nm (60 eV) with an energy resolution ($E/\Delta E = 50$)

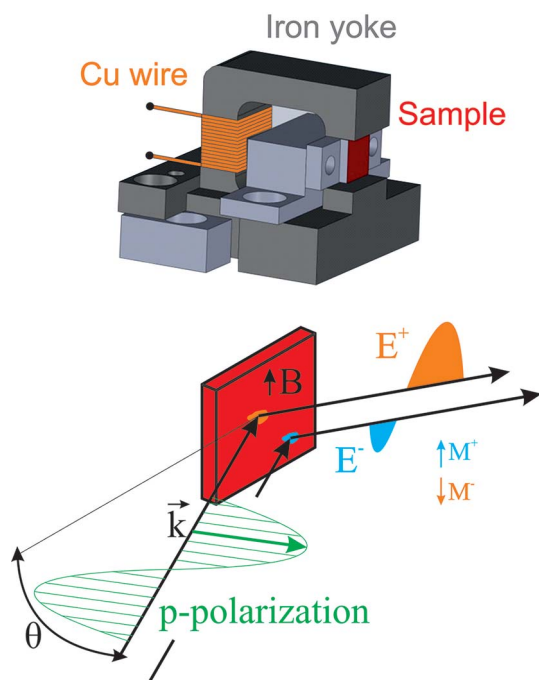


Figure 3
Top: sample holder for T-MOKE measurements. Bottom: T-MOKE geometry.

adapted to that of the beamline. According to the requirements that arise from use of reflection geometry, zone plates with a relatively long focal length of 15 mm for a photon energy $E = 60$ eV have been designed (Table 1). Apart from at 60 eV, the focal length f_E changes with the photon energy according to equation (1),

$$f_E = f(60 \text{ eV}) \frac{E}{60 \text{ eV}}. \quad (1)$$

The design and production process of the zone plates and the optical characterization of the plates has been described in detail in our earlier paper (Schümmer *et al.*, 2018). For imaging results presented in this paper we applied additional zone plates with absorbing Au rings on 50 nm thin Si_3N_4 membranes and free-standing Au zone plates with higher transmission (Table 1). The resolving power was measured using a Siemens star-like pattern, shown for the free-standing zone plate in Fig. 4.

2.5. Computer control

The microscope is controlled by a computer code developed with the LabVIEW programming tool. The code enables one-dimensional scans in the x - or y -direction, two-dimensional scans across the sample surface, zone-plate focus-adjustment and controlling the activation and the polarization settings of the electromagnet. During a measurement a single data point is recorded within 0.75 s. Therefore the step size and the total number of steps determine the data acquisition time. A typical image of 200×200 pixels thus requires a measurement time of 500 min (Figs. 4 and 6). For each data point the code records the positions of all nano-motors and the detector readouts.

Table 1

Parameters of the zone plates fabricated for use with the novel SRXM device at DELTA.

The zone plates were fabricated using the process discussed by Berges *et al.* (2007) for a photon energy of 60 eV (*if used). CBS: central beam stop.

Type	Focal length	Outer diameter	Outermost zone width	Numerical aperture	CBS diameter*
Au on Si_3N_4	15 mm	249 μm	1.25 μm	0.008	120 μm
Free-standing	15 mm	249 μm	1.25 μm	0.008	120 μm
PMMA	6.4 mm	325 μm	400 nm	0.021	–

After data acquisition a MATLAB code is used to create from the data a micrograph of the object.

2.6. Synchrotron radiation beamline

The SRXM microscope is installed at the bending-magnet beamline 12 at the DELTA synchrotron facility (Berges *et al.*, 2007). At this beamline the TGM-type monochromator covers the photon energy range between 20 eV and 100 eV with one fixed 600 lines mm^{-1} grating. The spectral resolution at 60 eV can be varied between 1.2 eV and 0.4 eV (Berges *et al.*, 2007). The illuminated area at the entrance side of the zone plate is about $1.5 \text{ mm} \times 1 \text{ mm}$. The degree of polarization was determined experimentally as a linear polarization $P_L = 0.71$

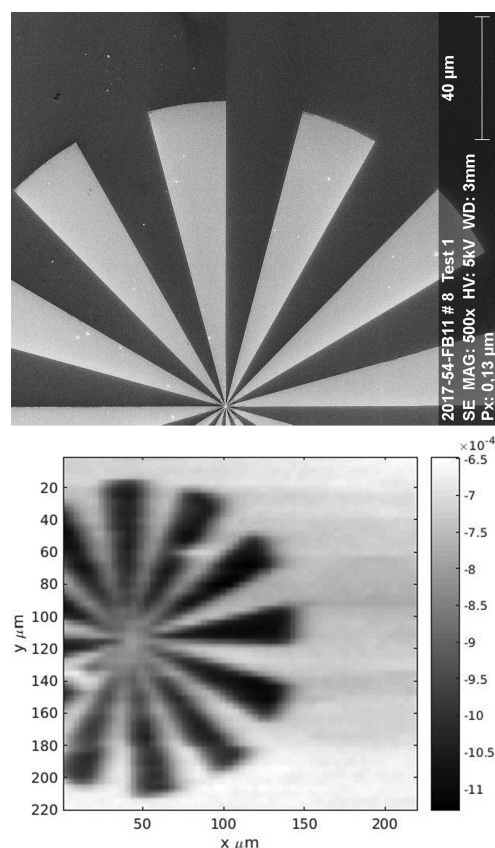


Figure 4
Top: electron microscopy image of the Siemens-star test pattern. Bottom: experimentally obtained SRXM image at 60 eV photon energy using the free-standing zone plate with zero-order beam stop. The figure indicates a zone plate resolution of $6 \mu\text{m}$ to $12 \mu\text{m}$.

and a circular polarization $P_C = 0.7$ at a photon energy of 60 eV (Tesch *et al.*, 2013).

Between the beamline monochromator and the SXR microscope a differential pumping stage is installed. It allows for the operation of our SXR microscope at a moderate high vacuum of 10^{-5} mbar and protects the beamline operating at ultra-high vacuum ($\leq 10^{-9}$ mbar). This setup enables easy and quick sample exchange in the SRXM of typically 60 min without operating a sophisticated *in situ* sample transfer.

2.7. Samples

For a particular zone plate, the resolution of the SXR microscope, when set up at DELTA beamline 12, is determined using a commercial Siemens star-like pattern (Fig. 4). This test sample consists of 75 nm-thick gold structures grown on a Si_3N_4 wafer with feature sizes from 0.2 μm to 50 μm . For imaging of magnetic domains, samples have been grown by molecular beam epitaxy at the Forschungszentrum Jülich. Two different types of magnetic samples have been fabricated. Firstly, a plain 10 nm thin epitaxial Fe (100) layer on a 150 nm-thick Ag buffer layer which was epitaxially grown on a GaAs (100) wafer using a 1 nm seed Fe layer (Bürgler *et al.*, 1997). This sample is covered with a 2 nm Au cap layer for passivation. The easy magnetic axes are in plane and aligned by 45° to the sample edge, respectively. The single Fe layer of this sample is used as a magnetic reference to monitor T-MOKE spectra.

A second type of magnetic sample was used to demonstrate the capability of magnetic depth profiling with the novel device. To this end, two nearly identical epitaxial Fe/Cr-wedge/Fe trilayer samples have been prepared, which consist of two 10 nm thin Fe layers separated by a 0.3–0.7 nm Cr wedge. The Fe/Cr-wedge/Fe sample was also covered by a 2 nm Au cap layer and grown on the same GaAs-based substrate system as described above. The two wedged-shaped samples were grown on differently cut GaAs wafer pieces and they thus differ in the orientation of their magnetic easy axes. The first wedge sample (K1) shows easy axes with 45° orientation to the sample edges; the second wedge sample (K2) shows easy axes oriented parallel to the sample edges, respectively.

3. Experimental results

3.1. Spatial resolution

The resolution ω of the novel SRXM device has been determined for the free-standing zone plate detailed in Table 1 using synchrotron radiation. For comparison, theoretically expected values can be deduced from the energy resolution of the synchrotron radiation and the beam parameter product as described in detail by Berges *et al.* (2007). Values are listed in Table 1. The experimental values have been deduced from images of the Siemens star-like test pattern (Fig. 4) giving resolutions in the range $6 \mu\text{m} \leq \omega \leq 12 \mu\text{m}$ [for details see equation (3) of Schümmer *et al.* (2018)]. The scanning step size was 1 μm according to the Nyquist–Shannon sampling theorem: structures down to 2 μm are thus measureable. The

sampling applied is therefore appropriate for the measurement. A detailed analysis is presented by Schümmer *et al.* (2018). The resolutions were measured with and without a central beam stop. The beam stop replaces the first ten inner zones of the plate. Zones and central beam stop are of identical thickness. As expected, the measured resolutions for the zone plate with and without central beam stop agree.

3.2. Magnetic- and element-selective imaging

One of the great advantages of our SRXM in the EUV is the element- and magnetization-selective imaging exploiting the energy-dependent reflectance. The element-sensitive imaging has been demonstrated on a chessboard pattern of 50 $\mu\text{m} \times 50 \mu\text{m}$ large Ti squares on a Si_3N_4 substrate. Images have been taken at different photon energies across the Ti 3s edge at 59 eV (Schümmer *et al.*, 2018). The chemical contrast between Si_3N_4 and Ti results from the increased reflectance at the Ti 3s edge, resulting in a strong contrast of about 35% between Ti and Si_3N_4 squares demonstrating the applicability of zone plate microscopy in reflection in the EUV range (Schümmer *et al.*, 2018).

For magnetic imaging the SRXM exploits T-MOKE geometry using linearly *p*-polarized synchrotron radiation. Here, the magnetic field is oriented perpendicular (transversal) to the scattering plane of linearly polarized light with the electric field oriented parallel to the scattering plane which means *p*-geometry (Fig. 3). The T-MOKE spectrum results from two spectra of the reflected intensities R_{\pm} with opposite magnetization direction $M+$ and $M-$ each oriented perpendicular to the scattering plane. Therefore, the external magnetic field was tuned to ± 16 mT and then switched off. Thus, the notations $M+$ and $M-$ denote the remanent magnetic states.

The strength of the T-MOKE signal and thus the strength of the sample magnetization is measured by the asymmetry parameter A_T expressed by

$$A_T = \frac{R_+ - R_-}{R_+ + R_-}. \quad (2)$$

Due to the magnetization-dependent reflectance the spectra R_+ and R_- differ from each other (Fig. 5) leading to a clear T-MOKE signal, as shown for a single Fe layer at photon energies across the Fe 3p edge (Fig. 5). These T-MOKE reflectance spectra of a homogeneous sample were monitored without zone plate optics.

As expected, the T-MOKE spectrum shows two peaks: one at 50.5 eV below the absorption edge (52.7 eV) and a second at 54.0 eV above the absorption edge. At each of these two energies magnetic imaging should create a strong contrast between corresponding magnetic domains with opposite transversal magnetization.

Furthermore, magneto-optical microscopy in reflection mode allows for a depth-resolved investigation of layered systems. This feature results from the energy-dependent penetration depth of the incident light.

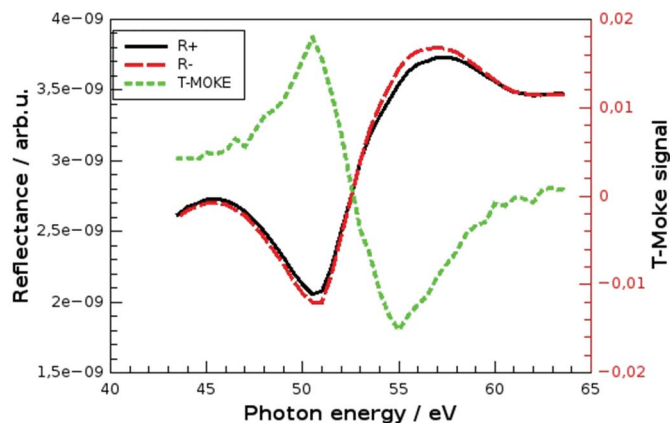


Figure 5
Reflected intensities of *p*-polarized light for magnetization directions $M+$ and $M-$, and resonant T-MOKE spectrum (dotted green line).

The penetration depth, which is defined as the distance after which the intensity is reduced to $1/e = 0.37$, serves as an approximate measure of the thickness of the contributing layer. Whereas a large penetration depth of 14.7 nm is expected for this sample at energies below the Fe $3p$ edge, at energies above the Fe $3p$ edge a shorter penetration depth of only 7.7 nm is predicted. These predictions are based on calculations using the online calculator of CXRO Berkeley (<http://www.cxro.lbl.gov/>) with optical constants from the Henke table (Henke *et al.*, 1993). This feature of an energy-dependent probing depth enables a qualitative estimation of the layers that contribute to the reflected light. In order to investigate predominantly the near-surface layers, photon energies just above the absorption edge can be used corresponding to a small penetration depth. In order to investigate both near-surface and buried layers, photon energies well below the absorption edge can be used giving a larger penetration depth. This approach has been explored in this work by imaging magnetic multi-layer samples with the structure Fe/Cr-wedge/Fe (samples K1 and K2).

The potential of magnetic imaging exploiting T-MOKE has been demonstrated for the Fe wedge sample K1. Results are

shown in Fig. 6. In order to reduce the scanning time, the scanning step width was set to 20 μm . The photon energy was set to 50.5 eV, well below the Fe $3p$ edge. The figure at the top of Fig. 6 shows the T-MOKE image resulting from the normalized difference of the two intensities measured for the reflected light. Identical sample position was assured. A coil current was applied that produced a maximum magnetic field of ± 16 mT each for 0.02 s. After this the current was switched off and the sample remained in the remanent state $M+$ or $M-$. For these situations the T-MOKE data were collected.

For an interpretation of the resulting micrograph in Fig. 6, three regions of different magnetic interlayer coupling along the Cr wedge may be considered. This is in agreement with the well established interpretation of such structures (Schäfer, 1995). On the left-hand side of the micrograph in Fig. 6 the Cr layer thickness is about 0.7 nm and an anti-ferromagnetic coupling of the two Fe layers can be expected. On the right-hand side of the micrograph, for a Cr layer thickness of 0.3 nm a ferromagnetic coupling of the Fe layers can be expected. In between these two thicknesses a transition region can be expected where the magnetizations of the layers are oriented perpendicularly to each other (90° coupling). This transition region is expected at a Cr thickness of about 0.5 nm and its magnitude depends on the interlayer roughness (Schmidt *et al.*, 1999).

According to this interpretation a maximum T-MOKE signal (blue or red) should occur on the right-hand side of the micrograph for ferromagnetic coupling and a vanishing T-MOKE contrast (black) for a vanishing total magnetization in the anti-ferromagnetic region on the left-hand side. Indeed, the recorded micrograph clearly shows this magnetization pattern, which is discussed in detail below.

Starting from the right of the micrograph in Fig. 6 going from $x = 3000 \mu\text{m}$ to $1700 \mu\text{m}$, the Cr thickness increases from 0.3 nm to about 0.45 nm. In this region a strong T-MOKE asymmetry is found with values up to $A_T = 0.06$ as expressed by an intense blue colour. Since the easy axes are oriented at 45° with respect to the sample edges, the total magnetization

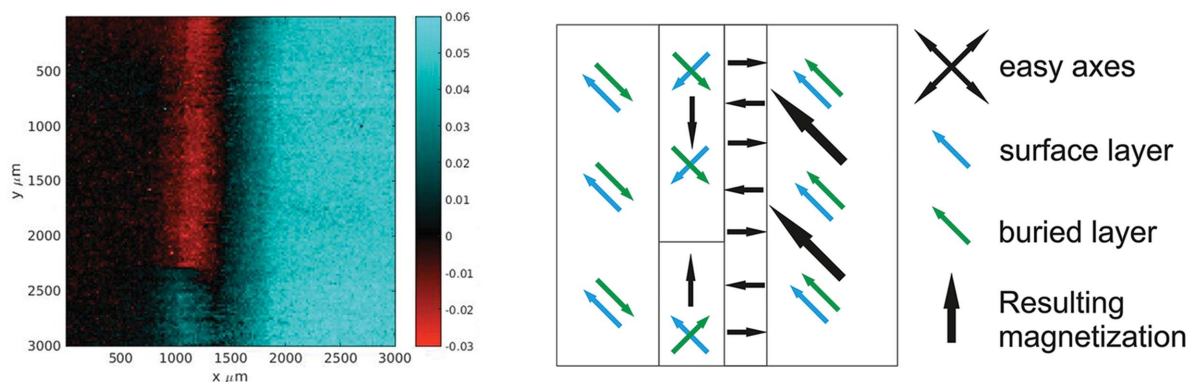


Figure 6
Left: SRXM micrograph recorded in T-MOKE mode of the magnetized sample K1. The thickness of the Cr wedge of this multilayer sample decreases from the left to the right of the micrograph from 0.7 to 0.3 nm. The intensity colour scale is given on the right of the micrograph. Right: sketch of the orientation of the magnetic easy axes and the magnetization directions in the Fe surface (blue) and Fe buried (green) layer of the sample using approximately the same *x*-axis as the micrograph on the left.

resulting from the two ferromagnetically coupled Fe layers is also oriented at 45° with respect to the edges. This is illustrated on the right of Fig. 6. The total magnetization is $2\mathbf{m}$, where \mathbf{m} represents the magnetization of a single 10 nm-thick Fe layer. Note that in this context only the vertical component of ($\sqrt{2}\mathbf{m}$) is relevant for the T-MOKE signal. Between $x = 1700 \mu\text{m}$ and $x = 1000 \mu\text{m}$ (Cr thickness between about 0.45 and 0.55 nm) the Cr layer is expected to mediate 90° -coupling. This yields the magnetizations of the upper and lower Fe layer that are perpendicular to each other with both of them still pointing along one of the two easy axes of the Fe(100) layer. In this region of the micrograph a colour change occurs: black on the right changes to red (or blue) on the left at about $x = 1200 \mu\text{m}$. The black region ($x \simeq 1300 \mu\text{m}$) shows a vanishing T-MOKE effect ($A_T = 0$). There may be two reasons for this: (i) vanishing total magnetization due to anti-ferromagnetic interlayer coupling or (ii) horizontally aligned total magnetization, since a T-MOKE signal requires the vertical magnetization component. As anti-ferromagnetic coupling is not expected for this Cr thickness of about 0.5 nm, the vanishing T-MOKE signal can be interpreted to be due to horizontal total magnetization. This results from adding 90° -coupled single layer magnetizations with opposite vertical components (see the sketch on the right in Fig. 6).

The intensity of the red (blue) colour in the upper (lower) part in the vertical region between $x = 1000 \mu\text{m}$ and $x = 1300 \mu\text{m}$ indicates a T-MOKE asymmetry of $A_T = \pm 0.03$. This contrast can be explained in a similar fashion as above by 90° -coupled single layer magnetizations with opposite horizontal components. They add up to a total magnetization in the vertical direction (see the sketch on the right of Fig. 6). The projection of the total magnetization in the vertical direction in the red (blue) part of this region is locally anti-parallel (parallel) to the direction of the corresponding projection of the total magnetization in the ferromagnetically coupled region for $3000 \mu\text{m} > x > 1700 \mu\text{m}$. However, the strength of the T-MOKE signal ($A_T = \pm 0.03$) is smaller than in the blue region on the very right of the micrograph. This cannot be explained by different amplitudes of the total magnetization,

since in both cases (ferromagnetic and 90° -coupling) the relevant vertical components are the same ($\sqrt{2}\mathbf{m}$). On the left-hand side of the micrograph, for $x < 1000 \mu\text{m}$ ($0.7 \text{ nm} > \text{Cr thickness} > 0.55 \text{ nm}$), anti-ferromagnetic coupling leading to a vanishing total magnetization and thus a predominantly black signal can be expected. This is indeed the case.

In order to investigate the respective role of the upper and lower magnetic Fe layer of the Fe/Cr-wedge/Fe sample in more detail, the different attenuation length of photons below and above the $3p$ absorption edge has been exploited and the relevant images were compared. This is shown for the K2 sample for which the easy axes are aligned parallel to the sample edges. The K2 sample has been installed with the thinner part of the wedge at the top and the thick end at the bottom of the image as shown in Fig. 7. Due to an inadvertent small tilt of the mounted sample the scanning directions are not exactly parallel to the sample edges. The actual orientation is sketched in the centre of Fig. 7. The scanning step width was set to $50 \mu\text{m}$, which is still sufficient to resolve magnetic domains but with reduced scanning time. In order to achieve magnetic contrast, a procedure was applied which differed in two points from that applied to the wedge sample K1 discussed above.

The sample K2 was not measured in remanence but was demagnetized by inverting the coil current consistently and reducing its absolute value, *i.e.* reducing the width of the hysteresis curve down to zero. This procedure is expected to create smaller magnetic domains than in the case of working in remanence. For K2 the magnetic contrast was deduced from two images: one monitored at photon energies near the Fe $3p$ – $3d$ resonance leading to a magnetic signal, and a second image monitored at a photon energy far away from the magnetic resonance energy serving as a non-magnetic topographical reference [see equation (3)]. Furthermore, depth-resolved magnetic information was deduced from two images containing magnetic information (I_M). The first image was obtained just below the resonance energy at 50.5 eV and the second image was obtained just above the resonance energy at 54 eV. The reference image without magnetic contribution (I_0)

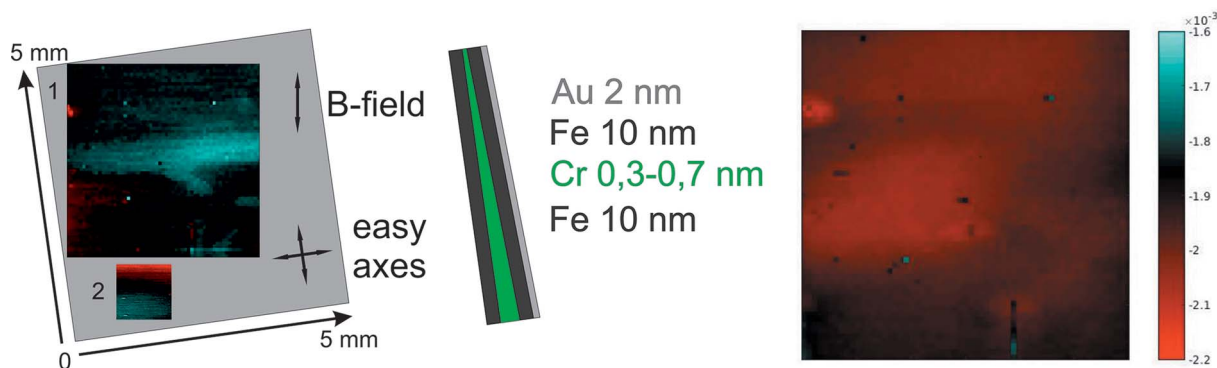


Figure 7 Left: difference images according to equation (3) of the Fe/Cr-wedge/Fe (K2) sample at 54 eV and 48 eV at two regions of the slightly tilted K2 sample (grey) with respect to the external vertical B-field. Region 1 corresponds to images in Fig. 8 and region 2 is linked to images in Fig. 9. Center: sketch of the Fe/Cr-wedge/Fe sample. Right: non-magnetic information of the topographic image obtained at 48 eV showing negligible magnetic signals. The size refers to region 1 showing a nearly homogeneous reflectance which is clearly distinct from the magnetic difference signals (left).

was monitored far below the resonance energy at 48 eV. The magnetic contrast was then calculated according to

$$A_{T0} = \frac{I_M - I_0}{I_M + I_0}. \quad (3)$$

For the interpretation of the magnetic micrograph obtained, again three types of magnetic coupling between the two Fe layers are assumed as discussed already for sample K1 above and according to Schäfer (1995). Consequently, a ferromagnetic region can be expected at the top (Fig. 7, left), an anti-ferromagnetic region at the bottom and a 90°-coupled region in the middle of the micrograph.

In Fig. 8 the magnetization directions are shown for the top Fe layer and the buried lower Fe layer separately. This information can be deduced from imaging above and below the 3*p* absorption edge as discussed below. The magnetic micrograph recorded above the Fe 3*p* resonance energy at 54 eV corresponds to a small probing depth and thus shows a stronger contribution of signals that originated from the near-surface region of the sample. In contrast, images taken at 50.5 eV below the 3*p* absorption edge show contributions from both the buried lower Fe layer beneath the Cr wedge and the upper Fe layer. This is because the penetration depth of photons is larger at these energies below the absorption edge.

In the top part of Fig. 8 a magnetic asymmetry signal can be seen. In the upper range, roughly 500 μm < *y* < 1500 μm, this

signal is a little bit weaker and in the following range, roughly 1500 μm < *y* < 2200 μm, it is stronger with values up to $A_T = 0.03$. These two regions of different magnetic contrast are interpreted as magnetic domains, since the non-magnetic image taken outside of 3*p* resonance at 48 eV (Fig. 7, right) does not show corresponding topographic features. Note that the calculation procedures of equations (2) and (3) differ with respect to the reference values $I(M+/-)$ and I_0 , which results approximately in $A_T = 2A_{T0}$. Thus, the asymmetry signals of the blue domains of Figs. 6 and 8 are of nearly identical strength.

The magnetic coupling of both Fe layers in the blue top part (500 μm < *y* < 2200 μm) can be interpreted as ferromagnetic, because the colour in the micrograph, *i.e.* the magnetic signal, does not change when switching from photon energies below (50.5 eV, probing both layers) and above the 3*p* edge (54 eV, probing predominantly the top layer). This means that both Fe layers show an identical orientation of their magnetizations. This interpretation is supported by the fact that the Cr wedge separating the Fe layers has in this part of the wedge a small thickness (<0.45 nm) causing ferromagnetic coupling. However, this upper blue region appears to be split into two domains with different alignment of the magnetization direction [Figs. 8(c) and 8(d)]. The strong T-MOKE asymmetry in the region 1500 μm < *y* < 2200 μm suggests a predominantly vertical alignment of the magnetization, parallel to the vertical

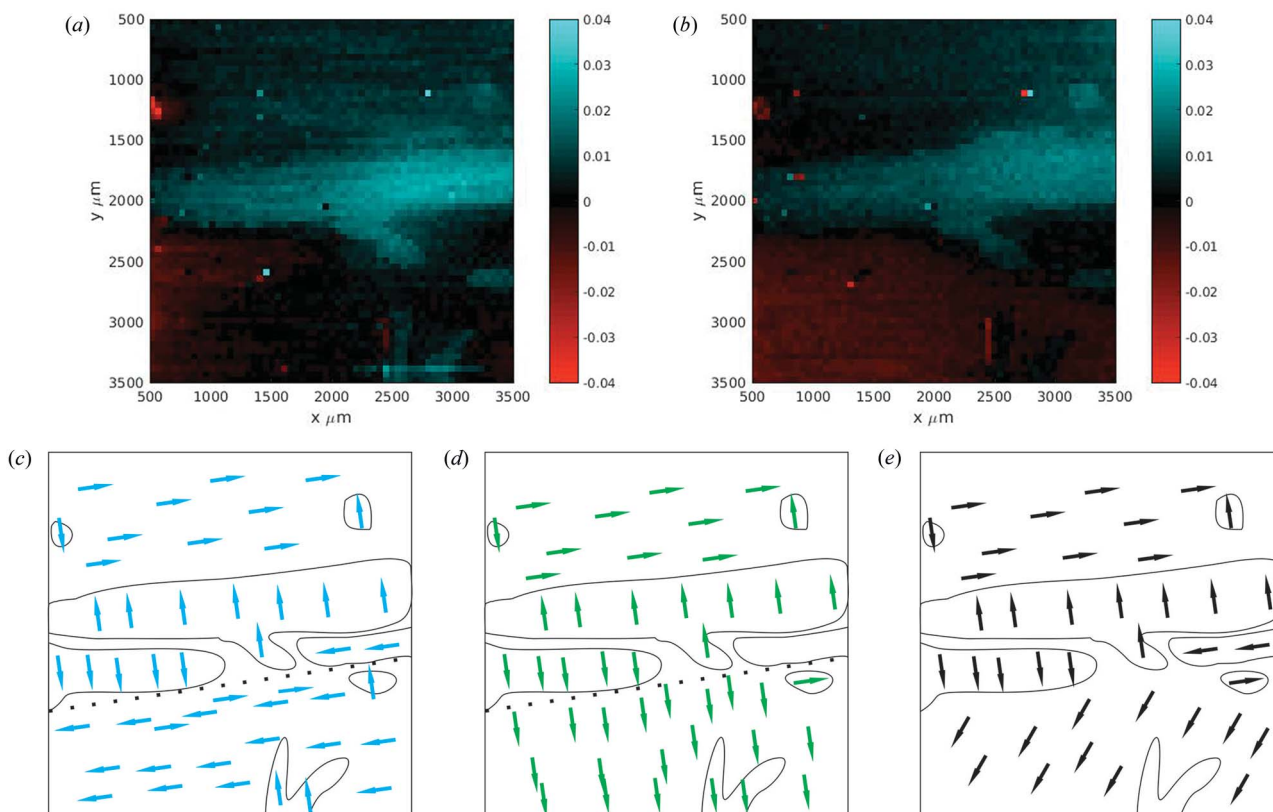


Figure 8

Micrographs of region 1 (Fig. 7) of the K2 sample, showing (a) predominantly the near-surface Fe layer magnetization mainly obtained at 54 eV and 48 eV via equation (3); (b) taken at 50.5 eV using equation (3), showing a combination of magnetic signals from surface and buried layer; (c) magnetic state of near-surface Fe layer; (d) magnetic state of buried Fe layer; (e) resulting total magnetization.

easy axes. It thus has a strong component parallel to the external magnetic field applied to demagnetize the sample prior to the T-MOKE measurements. In contrast, in the region $500\ \mu\text{m} < y < 1500\ \mu\text{m}$, additional horizontally aligned magnetizations must exist which do not contribute to the T-MOKE signal. Due to the fact that the sample has been tilted by about 20° and the proximity of this area to the sample edge (grey square in Fig. 7), a net vertical component of predominantly horizontally aligned moments exists and causes a weaker T-MOKE signal. This is in agreement with the demagnetization process applied to this sample K2.

In the central part of the sample (Fig. 7), which is found at the bottom of Fig. 8 at $y > 2500\ \mu\text{m}$, a 90° -coupling can be expected with perpendicular alignment of the magnetization directions in the domains of the lower and upper Fe layers (Schäfer, 1995). Therefore magnetic moments oriented transversal to the scattering plane should produce T-MOKE signals (blue or red), and domains with magnetic moments parallel to the scattering plane (black) should not contribute to the T-MOKE signal. Indeed, this can be identified. The micrograph in Fig. 8(a), taken at photon energies above the Fe $3p$ edge at 54 eV, reveals the Fe top layer and shows horizontally magnetized domains which do not contribute to the T-MOKE signal (black). For photon energies below the $3p$ edge at 50.5 eV in Fig. 8(b), both the top and bottom Fe layers are detected thus revealing a total magnetization with a transversal component contributing to the T-MOKE signal (red).

In Fig. 9 a feature at the bottom (Fig. 7) of the K2 sample at a Cr thickness exceeding 0.55 nm can be seen suggesting anti-ferromagnetic coupling. As observed by Schäfer (1995), the size of the magnetic domains decreases with increasing Cr spacer thickness, *i.e.* in the anti-ferromagnetic region of Fig. 9. Here, all bright red, black and blue domains are seen for imaging with photon energies above the Fe $3p$ edge (54 eV) (Fig. 9, left) revealing the magnetization of the top Fe layer. Switching to photon energies below the Fe $3p$ edge (50.5 eV), both anti-ferromagnetically coupled Fe layers are observed corresponding to vanishing total magnetization and vanishing T-MOKE signal (black).

It is important to realize that the interpretation of the T-MOKE signal for different probing depths is not straightforward.

The discussion above of the magnetizations of the upper and lower Fe layers of the multilayer samples on the basis of deduced penetration depth of the incident light should be considered as a qualitative approach only. Although the T-MOKE signal scales linearly with the relevant magnetization component, on the other hand the signal also depends on the absolute reflectance. The observed reflectance, however, results from the interference of light rays reflected at different layers (Valencia *et al.*, 2004). Thus, in a more detailed analysis, reflectivity simulations should be taken into account. Furthermore, the magneto-optical constants of the contributing layers and relevant interference effects of the reflected intensities need to be considered. Taking into account all interfaces and intensity, damping has the potential to yield a more quantitative description of the depth-profile of the magnetization in the multilayer sample.

4. Conclusion

We present the design and first results for a new type of scanning reflection X-ray microscope based on zone plate optics. The novel device exploits the element selectivity and the magnetic sensitivity of magneto-optical reflection in the EUV spectral range. The efficacy of this approach has been demonstrated with T-MOKE spectro-microscopy at the Fe $3p$ absorption edge. The new setup in particular allows for the characterization of thin magnetic layers on thick bulk samples and that of buried magnetic layers. Such characterization is not possible with established transmission X-ray microscopy which requires samples thinner than $2\ \mu\text{m}$. The applicability of the new device to magnetic materials has been demonstrated by imaging magnetic domains of Fe/Cr-wedge/Fe buried layer samples. In addition, the possibility of depth-profiling magnetic layered structures has been demonstrated for Fe/Cr/Fe multilayer samples where the Cr layer is a wedge. From T-MOKE signals for these samples the coupling of magnetic moments of the two adjacent Fe layers could be deduced. Results show a change from a parallel (ferromagnetic) coupling via a perpendicular orientation to an anti-parallel (anti-ferromagnetic) coupling as the thickness of the separating Cr wedge increases. Further improvement of the lateral

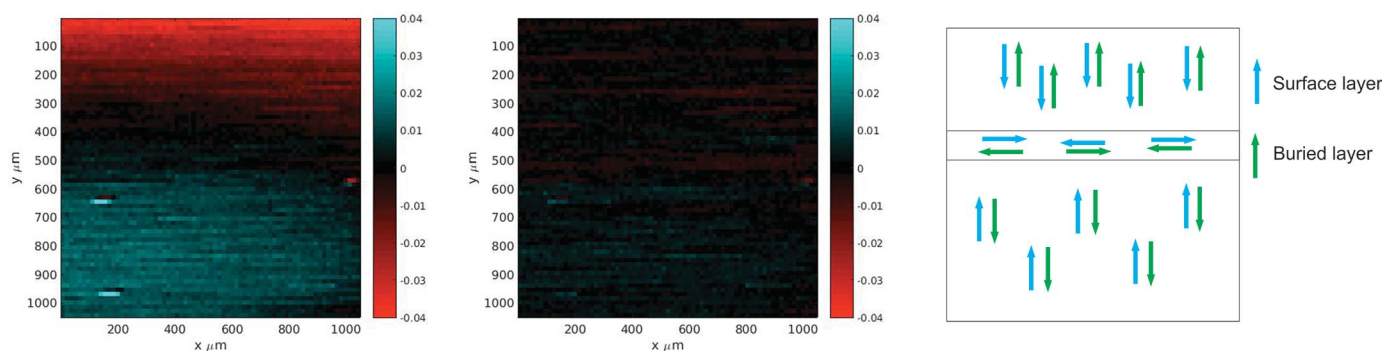


Figure 9 Micrograph of region 2 (Fig. 7) of the K2 sample. Left: micrograph obtained at 54 eV using equation (3) showing near-surface Fe layer contribution. Middle: micrograph obtained at 50.5 eV via equation (3) showing contributions of near-surface and buried Fe layers. Right: sketch of the magnetizations of the surface and buried Fe layer.

resolution of the new technique well below 1 μm is expected to be possible. This may be achieved by adapting the microscope design and selecting appropriate zone plates to suit undulator beamlines which offer improved energy resolution and better defined beam parameters than were accessible in this pioneering work.

Acknowledgements

We acknowledge the scientific support by M. Gilbert and technical contributions of O. Berges and co-workers from the mechanical workshop/FH Münster as well as the scientific staff of DELTA. We acknowledge valuable discussions and proofreading by H. Timmers.

Funding information

LJ acknowledges financial support from the Helmholtz Association for a Helmholtz professorship as a part of the Initiative and Networking Fund.

References

- Adam, J. F., Moy, J.-P. & Susini, J. (2005). *Rev. Sci. Instrum.* **76**, 091301.
- Aken, P. A. van, Styrsa, V. J., Liebscher, B., Woodland, A. B. & Redhammer, G. J. (1999). *Phys. Chem. Miner.* **26**, 584–590.
- Andrews, J. C., Meirer, F., Liu, Y., Mester, Z. & Pianetta, P. (2011). *Microsc. Res. Tech.* **74**, 671–681.
- Attwood, D. & Sakdinawat, A. (2017). *X-rays and Extreme Ultraviolet Radiation: Principles and Applications*, 2nd ed. Cambridge University Press.
- Berges, U., Sternemann, C., Tolan, M., Westphal, C., Weis, T. & Wille, K. (2007). *AIP Conf. Proc.* **879**, 30–33.
- Bracco, G. & Holst, B. (2013). *Surface Science Techniques*, ch. III. Springer.
- Bürgler, D. E., Schmidt, C. M., Schaller, D. M., Meisinger, F., Hofer, R. & Güntherodt, H.-J. (1997). *Phys. Rev. B*, **56**, 4149–4158.
- Denbeaux, G., Fischer, P. & Salmassi, F. (2005). *IPAP Conf. Ser.* **7**, 375–386.
- Hecker, M., Oppeneer, P. M., Valencia, S., Mertins, H. & Schneider, C. M. (2005). *J. Electron Spectrosc. Relat. Phenom.* **144–147**, 881–884.
- Henke, B., Gullikson, E. & Davis, J. (1993). *Atomic Data and Nuclear Data Tables*, <http://xdb.lbl.gov/>.
- Hubert, A. & Schäfer, R. (1998). *Magnetic Domains – The Analysis of Magnetic Microstructures*. Springer.
- Johnson, A. S., Avni, T., Larsen, E. W., Austin, D. R. & Marangos, J. P. (2019). *Phil. Trans. R. Soc. A*, **377**, 20170468.
- Kirz, J., Jacobsen, C. & Howells, M. (1995). *Q. Rev. Biophys.* **28**, 33–130.
- Kuch, W., Schäfer, R., Fischer, P. & Hillebrecht, F. U. (2015). *Magneto-Optical Effects*. Springer.
- Kuneš, J., Oppeneer, P. M., Valencia, S., Abramssohn, D., Mertins, H., Gudat, W., Hecker, M. & Schneider, C. M. (2004). *J. Magn. Magn. Mater.* **272–276**, 2146–2147.
- Mann, K., Holburg, J., Lange, S., Müller, M. & Schäfer, B. (2019). *Proc. SPIE*, **10957**, 109571H.
- Mertins, H., Abramssohn, D., Gaupp, A., Schäfers, F., Gudat, W., Zaharko, O., Grimmer, H. & Oppeneer, P. M. (2002). *Phys. Rev. B*, **66**, 184404.
- Mertins, H., Valencia, S., Abramssohn, D., Gaupp, A., Gudat, W. & Oppeneer, P. M. (2004). *Phys. Rev. B*, **69**, 064407.
- Mertins, H.-C., Valencia, S., Gaupp, A., Gudat, W., Oppeneer, P. & Schneider, C. (2005). *Appl. Phys. A*, **80**, 1011–1020.
- Mobilio, S., Bischerini, F. & Meneghini, C. (2015). *Synchrotron Radiation*, ch. 15. Springer-Verlag.
- Oppeneer, P. M., Mertins, H., Abramssohn, D., Gaupp, A., Gudat, W., Kuneš, J. & Schneider, C. M. (2003). *Phys. Rev. B*, **67**, 052401.
- Ruoss, S., Stahl, C., Bayer, J., Schuetz, G., Albrecht, J. & Laviano, F. (2016). *IEEE Trans. Appl. Supercond.* **26**, 7500606..
- Schäfer, R. (1995). *J. Magn. Magn. Mater.* **148**, 226–231.
- Schmidt, C. M., Bürgler, D. E., Schaller, D. M., Meisinger, F. & Güntherodt, H. (1999). *Phys. Rev. B*, **60**, 4158–4169.
- Schümmer, A., Mertins, H., Schneider, C. M., Adam, R., Trelenkamp, S., Borowski, R., Juschkina, L. & Berges, U. (2018). *Appl. Opt.* **58**, 1057–1063.
- Späth, A., Raabe, J. & Fink, R. H. (2015). *J. Synchrotron Rad.* **22**, 113–118.
- Stöhr, J. & Siegmann, H. Ch. (2006). *Magnetism: From Fundamentals to Nanoscale Dynamics*. Springer.
- Tesch, M. F., Gilbert, M. C., Mertins, H., Bürgler, D. E., Berges, U. & Schneider, C. M. (2013). *Appl. Opt.* **52**, 4294–4310.
- Tesch, M. F., Legut, D., Mertins, H., Gilbert, M. C., Jansing, C., Hamrle, J., Ruzs, J., Oppeneer, P. M., Bürgler, D. E., Schneider, C. M., Gaupp, A. & Berges, U. (2014). *Phys. Rev. B*, **89**, 140404.